ELSEVIER

Materials Science and Engineering A201 (1995) 88–102

MATERIALS SCIENCE & ENGINEERING A

Mechanical properties and microstructure of cast oxide-dispersion-strengthened aluminum

A.M. Redsten[a], E.M. Klier[b], A.M. Brown[b], D.C. Dunand[a]

[a]*Department of Materials Science and Engineering, Massachusetts Institute of Technology, Cambridge, MA 02139, USA*
[b]*Chesapeake Composites Corporation, 239 Old Churchman's Road, New Castle, DE 19720, USA*

Received 14 October 1994; in revised form 1 December 1994

Abstract

Oxide-dispersion-strengthened aluminum containing 25 vol.%, 0.28 μm, alumina dispersoids was fabricated by pressure infiltration. The mechanical properties at room and elevated temperature are presented for both as-cast, coarse-grained materials and extruded, fine-grained materials. Although the room temperature yield strength is low (about 60 MPa), the 0.2% proof stress and ultimate tensile stress are much higher (about 200 MPa and 330 MPa respectively) as a result of the very high strain hardening rate. However, the initially high strain hardening rate decreases with strain. This behavior is explained by extending a model by Ashby for dilute dispersion-strengthened metals to the case of a matrix containing a large volume fraction of large particles, whereby the interaction of primary glide dislocations with secondary loops punched by dispersoids is considered.

Keywords: Mechanical properties; Microstructure; Aluminum; Dispersion strengthening

1. Introduction

Particles formed on heat treatment of precipitation-hardened aluminum alloys impede the motion of dislocations, imparting excellent ambient temperature mechanical properties to these alloys. However, most precipitates are not chemically stable at elevated temperature, leading to their coarsening or dissolution, and a concomitant decrease in alloy strength [1,2]. Rapidly solidified alloys typically show better strength retention at elevated temperatures than precipitation-hardened alloys, due to the higher stability and lower solubility of the intermetallic dispersoids in the matrix [3,4], but still weaken considerably at high temperature due to coarsening of the second phase.

Dissolution and coarsening can be eliminated by introducing chemically stable, insoluble dispersoids into aluminum. Sintered aluminum powder (SAP) materials, produced by densification of oxidized aluminum powders, exhibit better strength than precipitation-strengthened alloys at temperatures above about 200 °C [5–7]. Moreover, the alumina flakes, about 30–70 nm in size, pin grain boundaries on recrystallization, resulting in stable fine grains and additional grain boundary strengthening. Aluminum alloys produced by mechanical alloying show better ductility, yield and tensile strength at ambient and elevated temperature than SAP materials with the same amount of alumina [8–11]. This improvement is a result of the more homogeneous distribution, and more equiaxed shape, of the fine dispersoids (30–40 nm aluminum carbide and oxide), as well as the finer grain size of the matrix (0.2–0.5 μm).

Unlike alloys containing submicrometer dispersoids, the main strengthening mechanisms for discontinuously reinforced metal matrix composites (MMCs) containing particulates, 1–100 μm in size, are load transfer from the matrix to the reinforcement, constrained matrix flow and dislocation strengthening by loops punched due to the difference between the thermal expansion of the two phases [12]. Orowan strengthening, one of the main strengthening mechanisms in alloys with submicrometer dispersoids, is negligible in MMCs, due to the large interparticle distance resulting from the large reinforcement size [13,14]. At high temperatures, the strength of discontinuously reinforced MMCs de-

SSDI 0921-5093(94)09741-0

creases, since load transfer and constrained flow decrease due to interface decohesion and matrix creep, and dislocation strengthening is reduced by matrix recovery, matrix recrystallization and reduction of thermal mismatch [15].

Only recently have researchers explored particle reinforcements smaller than 1 μm for MMCs. Geiger and Walker [16] found that the strength and ductility at room temperature of Al-6013 with 20 vol.% SiC particles increased as the particle size decreased, except for the composites with the finest particles investigated (0.7 μm SiC). The decrease in ductility for the finer sized particles was attributed to particle clustering during powder metallurgy processing. Tan et al. [17] reported a modest increase in proof stress with 20 vol.% of 0.08 μm SiC particles added to Al-AA8090, and an almost twofold decrease in ductility to a still useful value of about 7%, resulting from uneven reinforcement distribution and residual porosity. Arsenault [18] examined Al-1100 containing 20 vol.% SiC spherical particles, 0.5 μm in diameter. The composite proof stress was found to be 207 MPa, a large increase compared with the value of 34 MPa reported for the unreinforced matrix. Hong et al. [19] mechanically alloyed commercially pure aluminum with 10, 20 and 30 vol.% SiC particles as small as 0.66 μm. The much improved distribution of SiC resulted in high compressive proof strength values (309 MPa, 420 MPa and 524 MPa respectively). Yi et al. [20] synthesized 10–21 vol.% alumina and titanium carbide particles about 0.5 μm in size during consolidation of Al-A2219 powders. As the reinforcement content increased, the proof and ultimate tensile strength increased markedly, but the ductility decreased to less than 1% as a result of residual porosity and intermetallic formation.

In all of the above studies, the composites were fabricated by powder metallurgy and thus exhibited small, but unspecified, amounts of fine alumina particles originating from the oxidized surface of the aluminum powders, the strengthening contribution of which can be substantial. A few investigators have examined the properties of cast composites with submicrometer particles which do not contain these extraneous alumina particles. Aikin and Christodoulou [21] fabricated manganese-free Al-2124 with 0.3 μm TiB_2 particles and pure aluminum containing 0.7 μm TiC particles by the XD™ process. Although no ductility values were reported, the proof stress was found to increase with the particulate volume fraction, reaching values of 360 MPa for 15 vol.% TiB_2 in Al-2124 after a T4 temper and 125 MPa for 15 vol.% TiC in aluminum. Shanker et al. [22] infiltrated preforms containing 43–62 vol.% TaC particles (0.1–1 μm) with unalloyed liquid aluminum, resulting in composites with tensile proof stress values between 80 and 140 MPa and high ductility values between 7% and 19%. In a companion study, Muscat et al. [23] infiltrated sintered preforms of TiC (50–85 vol.% of 0.8 μm particles) with unalloyed aluminum. With increasing TiC content, the proof strength increased from 250 MPa to 475 MPa, while the ductility decreased from 5% to 0%.

In the present study, we investigate the mechanical properties and microstructure of oxide-dispersion-strengthened (ODS) aluminum materials produced by liquid metal pressure infiltration of alumina particles. The ODS material exhibits unsintered submicrometer ceramic particles with a size (0.28 μm) and volume fraction (25 vol.%) different from those of MMCs (which, with the exceptions noted above, typically have coarser particles [16,24,25]), and mechanically alloyed or rapidly solidified aluminum materials (with lower volume fractions of finer particles). Furthermore, we investigate materials with both millimeter-sized grains, rarely achievable with mechanically alloyed or rapidly solidified materials, and micrometer-sized grains, rarely achievable with MMCs.

2. Experimental procedures

Binder-free preforms were fabricated with 25 vol.% ± 0.5 vol.% of 99.8% pure α-Al_2O_3 particles. The particle size was 0.28 ± 0.03 μm (30% of the particles were smaller than 0.15 μm and 10% were larger than 0.32 μm). The preforms were pressure infiltrated with liquid aluminum (99.9% Al or Al–2.5%Mg), and solidified directionally under pressure. Some of the as-cast cylindrical billets, respectively labeled as ODS-Al and ODS-AlMg, were further extruded into rods with an extrusion ratio of about 12 at the temperatures given in Table 1. Machining was performed using high-speed steel or carbide cutting tools.

The as-cast material was characterized at room temperature by tensile testing, using round, tapered-seat, tensile bars with a diameter of 6.3 mm outfitted with an extensometer. Fracture surfaces were examined with a scanning electron microscope (JEOL model JSM 840) operating at 20 kV. Extruded samples were tested in tension at room and elevated temperature. The fracture toughness of as-cast specimens was measured at room temperature according to ASTM E-1304-89.

Hardness testing of diamond polished samples was performed with a Vickers DPH indenter outfitted with a furnace. The samples were held isothermally for 30 min at the highest test temperature prior to a hardness indentation. A 1.245 kgf load was then applied to the sample for 15 s and the operation repeated at monotonically decreasing temperatures. Two to five hardness measurements were made at each temperature and averaged. A grain growth experiment was conducted on 550 °C extruded ODS-Al by annealing in air at 650 °C for 139 h.

Table 1
Engineering tensile properties of as-cast and extruded ODS samples (average of at least two samples)

Material	State	Temperature (°C)	Proof stress[a] (MPa)	UTS (MPa)	Ductility (%)
ODS aluminium					
Al/25% Al_2O_3	As-cast	22	170	330	4.7[b]
Al/25% Al_2O_3	Extruded at 550°C	22	225	340	9.4
	Extruded at 440°C	22	205	345	11.0
	Extruded at 440°C	150	190	245	11.0
	Extruded at 440°C	260	160	170	12.0
Al–2.5 Mg/25% Al_2O_3	Extruded at 370°C	22	320	390	6.5
	Extruded at 370°C	93	265	335	8.7
	Extruded at 370°C	150	210	275	16.2
Unreinforced matrix					
Al–99.8% (1080) [26]	O	22	20	60	45
Al–2.5 Mg (5252) [27]	H25[c]	22	170	235	11

[a]Measured at 0.2% plastic strain. [b]Average of four samples, varying between 3.2% and 6%. [c]Strain hardened and partially recovered.

Metallographic samples were polished using standard techniques, and examined without etching by optical microscopy. The as-cast, polished samples were anodized in Barker's etch for approximately 30 s at a voltage of 20 V. Samples for transmission electron microscopy (TEM) were prepared by a combination of mechanical grinding, dimpling and ion milling. Bulk material was first sectioned with a low-speed diamond saw and ground to a thickness of approximately 400 μm. Disks, 3 mm in diameter, were then punched and dimpled with a 3 μm diamond slurry to a thickness of less than 50 μm. Finally, thinning to perforation was conducted using a Gatan Dual Ion Mill operating at 6 kV on a cooled sample stage. The thinned samples were observed in a JEOL 200 CX transmission electron microscope operating at 200 kV.

3. Experimental results

3.1. Processing and microstructures

Pressure infiltration results in complete penetration of the preform by the liquid metal, with no macroscopic preform disruption or compression. Directional solidification under pressure leads to the elimination of solidification shrinkage and macroporosity in the as-cast samples (Fig. 1). The sample consists of alumina-rich regions about 1 μm wide, separated by aluminum-rich channels of the same scale. A few aluminum-rich regions up to 10 μm in diameter are also visible in Fig. 1. The anodized, as-cast material exhibits very large grains, 2–10 mm in size, while the 550 °C extruded material has a much finer grain size: an average of ten grain areas gives 2.0 μm^2, corresponding to a grain size of about 1.3 μm. Alumina particles are located with higher frequency at grain boundaries than in the grain interior. The grain size after annealing at 650 °C for 139 h is approximately 1.8 μm.

Figs. 2–6 illustrate the microstructure of the samples observed by TEM. Figs. 2 and 3 show the particle distribution after infiltration and extrusion at 550 °C respectively. The as-cast sample (Fig. 2) exhibits clusters of alumina particles, separated by aluminum channels, the size of which corresponds to those of the alumina- and aluminum-rich regions observed by optical microscopy (Fig. 1). Although the extruded sample shows an improved particle distribution, particle clusters are still visible (Fig. 3). For both samples, the alumina-rich regions are pore free and the equiaxed particles are in the size range of the alumina powders before infiltration indicating that neither sintering nor coarsening of the alumina particles takes place during processing. Fig. 4 shows dislocation tangles at the border between an alumina cluster and an aluminum-rich region in the as-cast material. The dislocation density was found to increase closer to the alumina-rich regions. In the extruded sample, the dislo-

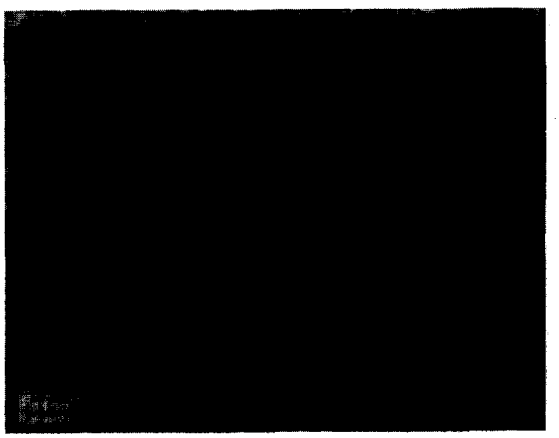

Fig. 1. Optical micrograph of as-cast ODS-Al showing complete infiltration and regions with varying alumina content.

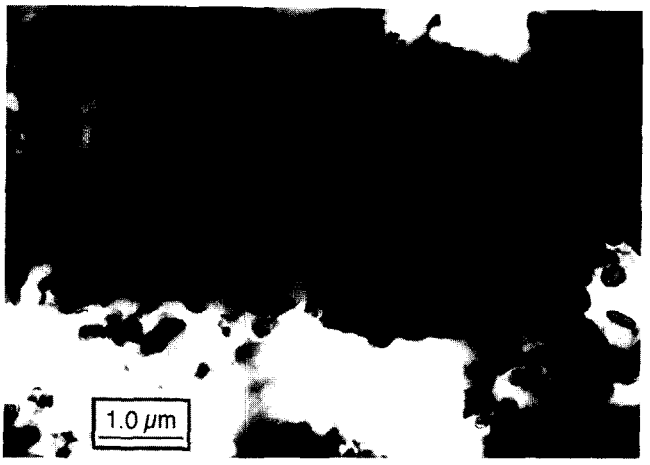

Fig. 2. Transmission electron micrograph of as-cast ODS-Al showing particle distribution and complete infiltration.

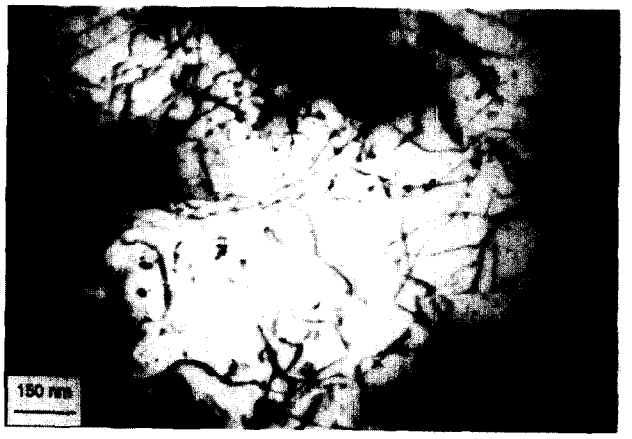

Fig. 4. Transmission electron micrograph of as-cast ODS-Al showing dislocation structure at the border between an aluminum-rich region and an alumina-rich region.

cation density is generally lower than in the as-cast sample. Figs. 5 and 6 show the dislocation structure of the samples deformed to fracture at room temperature. The as-cast sample shows subgrains in the aluminum-rich regions (Fig. 5), while the fine-grained, extruded samples exhibit very few subgrains. Fig. 6 shows a pile-up of dislocations interacting with particles. Finally, both Figs. 5 and 6 show dislocations emitted by an alumina particle.

3.2. Mechanical properties

Engineering tensile properties (average of at least two samples) of all tested samples are summarized in Table 1. Compared with the respective unreinforced matrices, also listed in Table 1, the ODS materials exhibit significantly higher proof and ultimate stress values, but lower ductilities. However, the yield stress, determined as the first detectable deviation from the linear portion of the stress–strain curve, is relatively low: 60 MPa for as-cast ODS-Al compared with 20 MPa for 99.8% pure aluminum [26]. The 0.2% proof stress is many times higher than the yield stress as a result of the strong strain hardening discussed in the next section.

Extrusion of the as-cast ODS-Al material improves the room temperature engineering mechanical properties: the proof stress is increased by 21%–32%, the ultimate tensile strength by about 3% and the ductility is more than doubled. The yield stress of ODS-Al extruded at 550 °C is, however, comparable with that of the as-cast sample (30–60 MPa). Compared with extruded ODS-Al, the proof and ultimate stress of extruded ODS-AlMg is increased, most probably as a result of solid solution strengthening. Similar strength increases in Al–SiC MMCs have been observed on solid solution of the matrix [28]. Furthermore, the elastic modulus and Poisson's ratio of extruded ODS-AlMg were measured by the ultrasonic method as $E = 110$ GPa and $\nu = 0.318$ respectively.

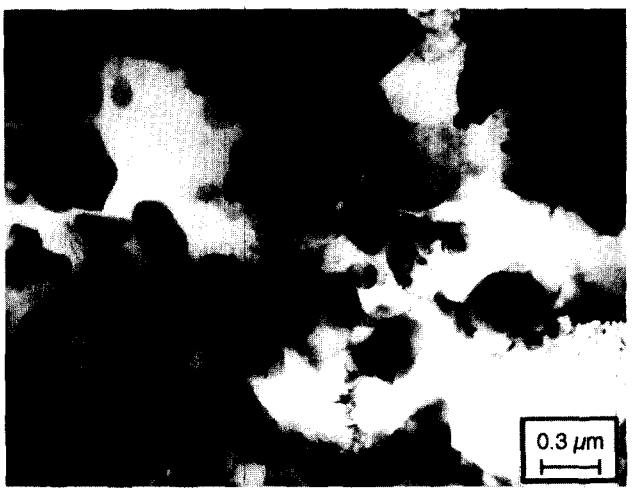

Fig. 3. Transmission electron micrograph of ODS-Al extruded at 550 °C showing improved particle distribution.

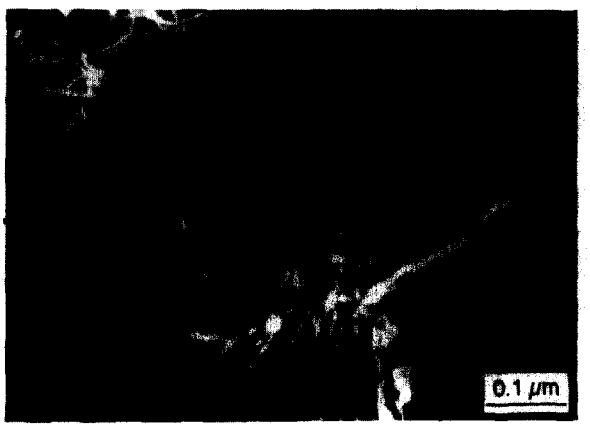

Fig. 5. Weak-beam dark-field transmission electron micrograph of as-cast ODS-Al deformed at room temperature, showing an alumina particle interacting with dislocations and a portion of a subgrain boundary.

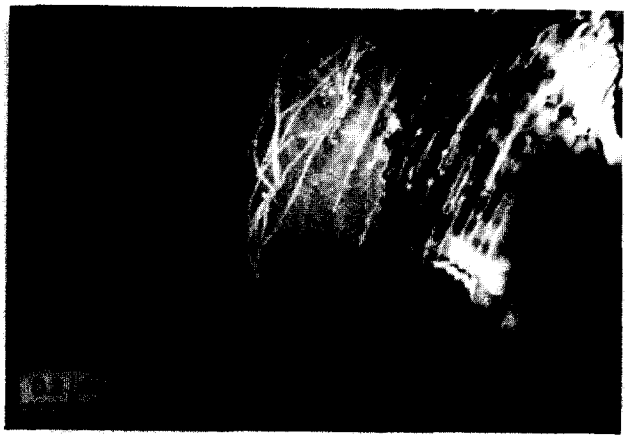

Fig. 6. Weak-beam dark-field transmission electron micrograph of ODS-Al extruded at 550 °C and deformed at room temperature, showing dislocations bowing from an alumina particle as well as a dislocation pile-up.

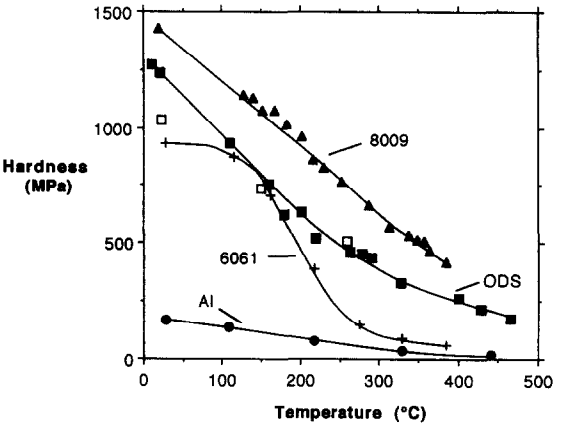

Fig. 8. Temperature dependence of the hardness for as-cast ODS-Al, pure aluminum, dispersion-strengthened alloy 6061 and rapidly solidified AA-8009 (Al–8Fe–1V–1.2Si). Open symbol values are calculated from UTS valves.

The fracture toughness of as-cast ODS-Al is $K_{1C} = 18$ MPa $m^{1/2}$. The fracture surface of as-cast ODS-Al exhibits microdimples, 0.2–1 μm in size (Fig. 7(a)), with larger dimples around agglomerates. The dispersoids found within these dimples range in size from about 0.1 μm to about 0.4 μm, although a few agglomerates as large as 1 μm are also observed. Fracture of one ODS-Al sample extruded at 550 °C initiated at the outer edge of the specimen and propagated perpendicularly to the tensile axis in a 45° zig-zag fashion. The peak-to-peak spacing of the zig-zagging front is 50–100 μm near the initiation point (Fig. 7(b)). Closer to the center of the sample, the front fans out and becomes more diffuse; a macroscopic cup-cone fracture is found around 75% of the circumference. Both the sides of the zig-zags and the face of the shear lip exhibit microdimples similar to those in Fig. 7(a).

Hot hardness values for as-cast ODS-Al, pure aluminum, precipitation-strengthened aluminum alloy 6061 and rapidly solidified aluminum alloy 8009 are compared in Fig. 8. Fig. 9 shows the tensile properties at elevated temperature of extruded ODS-Al and ODS-AlMg: the ultimate tensile strength is halved between room temperature and 250 °C, and the ductility is almost unchanged, except for an increased value for ODS-AlMg at 150 °C.

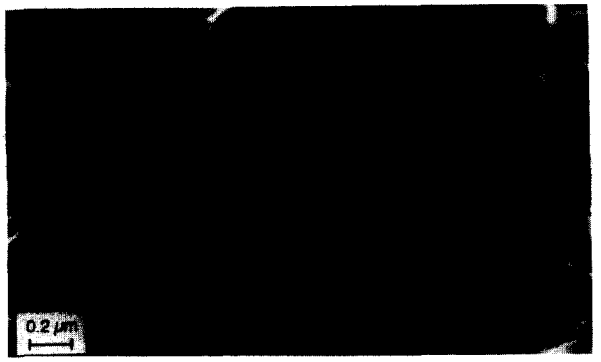

(a)

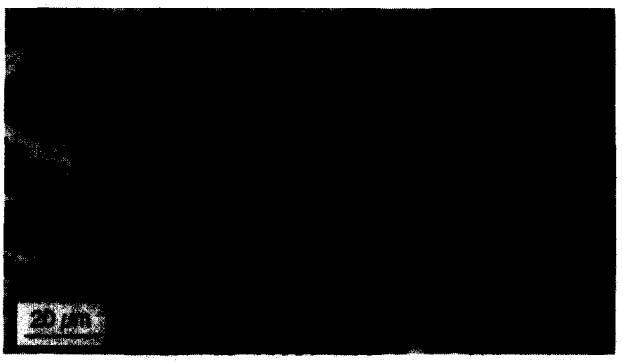

(b)

Fig. 7. Fracture surface of ODS materials: (a) high magnification of the as-cast material, showing small dimples containing individual particles; (b) low magnification of the extruded (550 °C) material, showing the zig-zag nature of the fracture path. Micrograph taken parallel to the direction of crack propagation.

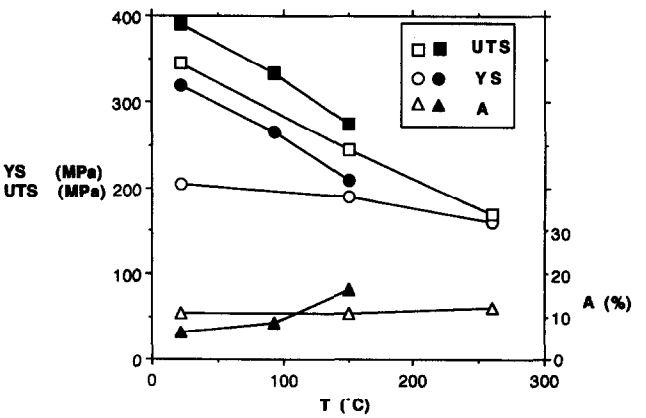

Fig. 9. Temperature dependence of the mechanical properties of ODS-Al extruded at 440 °C (open symbols) and ODS-AlMg (filled symbols) extruded at 370 °C.

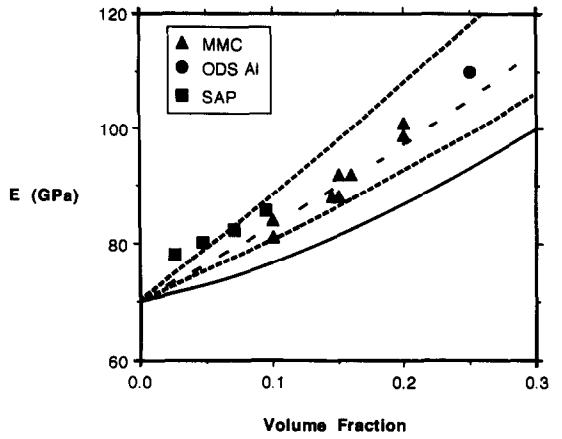

Fig. 10. Elastic modulus as a function of alumina volume fraction for ODS-AlMg, SAP aluminum [32] and aluminum MMCs [31]. The Halpin–Tsai equation (Eq. (A2)) is shown as a widely spaced broken line, the shear lag prediction (Eq. (A1)) as a full line and Hashin's bounds (Eq. (A6)) as finely spaced broken lines.

4. Discussion

4.1. Elastic modulus

The elastic modulus for ODS-AlMg, $E = 110$ GPa, is 57% higher than that of the unreinforced matrix, corresponding to an increase of more than 40% in specific stiffness. The measured value is also significantly higher than values for typical rapidly solidified or mechanically alloyed alloys. Rapidly solidified alloys containing submicrometer intermetallic particles exhibit Young's moduli below 90 GPa for volume fractions up to 30 vol.% [29,30], because intermetallic second phases in these alloys have an elastic modulus significantly smaller than alumina. Mechanically alloyed aluminum containing 14 vol.% aluminum oxide and carbide has a Young's modulus of 70 GPa [9], i.e. similar to unreinforced pure aluminum [9]. Therefore, for mechanically alloyed aluminum, either aluminum carbide exhibits very low stiffness or elastic load transfer is not operative as a result of interface decohesion.

Fig. 10 shows the elastic modulus of various alumina-reinforced aluminum alloys: MMCs with alumina particles about 10 μm in size [31], SAP with alumina dispersoids less than 0.1 μm [32] and ODS-AlMg with 0.28 μm alumina particles, investigated in this study. For all materials with volume fractions above 5%, the measured elastic moduli are within Hashin's bounds [33], close to the Halpin–Tsai prediction [34] and higher than the lower bound given by the shear-lag theory [12] (Appendix A). Deviations for SAP materials at low volume fractions in Fig. 10 can be explained by the orientation and/or clustering of the alumina platelets as a result of extrusion, increasing the elastic modulus in the extrusion direction compared with equiaxed, dispersed inclusions of the same volume fraction. Aluminum stiffening takes place for all materials considered (SAP, ODS and MMC aluminum), indicating good interfacial bonding and efficient load transfer, independent of alumina particle size.

4.2. Yield strength

The ODS materials examined in this study fall between two well-defined regimes: MMCs with particles larger than 1 μm and mechanically alloyed alloys with particles smaller than 0.1 μm. The strengthening mechanisms for these two regimes are discussed below, from both a dislocation micromechanics and a continuum mechanics viewpoint.

4.2.1. Dislocation micromechanics models

The main strengthening contribution for MMCs with large equiaxed particles stems from the prismatic dislocation loops generated by the difference between the thermal expansion of the two phases [35–38], which results in forest hardening. On the other hand, for aluminum-containing particles smaller than about 0.1 μm, dispersion strengthening (Orowan strengthening) and, if the material is fine grained, boundary strengthening (Hall–Petch strengthening) are dominant [39]. Strengthening by the prismatic loops punched due to thermal mismatch strains is not expected for mechanically alloyed aluminum or SAP with particles smaller than a critical diameter d^*, defined as the diameter for which a particle punches a single loop for each of the active glide directions. Using a simple one-dimensional model, which was found to match experimental data in the model system AgCl/glass [40], d^* is estimated as

$$d^* = \frac{b}{\Delta\alpha\Delta T} \tag{1}$$

where $b = 0.286$ nm [41] is the Burger's vector of aluminum, $\Delta\alpha = 1.5 \times 10^{-5}\ K^{-1}$ is the difference between the coefficients of thermal expansion (CTE) for the system Al/Al_2O_3 [42] and $\Delta T = 250$ K is the temperature excursion (the latter value is discussed in Appendix B).

For ODS-Al, the alumina particles are expected to provide both dispersion strengthening (found in mechanically alloyed aluminum or SAP, but not in typical MMCs due to the large interparticle distance) and forest strengthening by thermal mismatch punching, since the particle diameter ($d = 0.28$ μm) is larger than the critical value calculated from Eq. (1) ($d^* = 0.08$ μm). This is confirmed by the high dislocation densities observed near particles in undeformed samples (Fig. 4). However, each of these two strengthening mechanisms (Orowan and forest hardening, evaluated in Appendix B) yields a higher value than the yield stress increase measured for the as-cast samples, $\Delta\sigma = 40$ MPa. This discrepancy can be qualitatively justified by the inhomogeneous distribution of particles at the microscopic

level, as shown in Figs. 1 and 2. First, Orowan strengthening is sensitive to particle spacing (Eq. (B1), Appendix B) and thus to particle distribution. If dislocations are gliding in the aluminum-rich regions, while bypassing the alumina-rich regions as a whole, Eq. (B1) (Appendix B) gives $\sigma_1 = 43$ MPa for an effective particle size of 1 μm. Similarly, in mechanically alloyed aluminum (which is expected to exhibit a significantly more uniform particle distribution than as-cast ODS-Al), only about 70% of the particles are found to be effective in strengthening, as a result of inhomogeneous particle distribution [9,43]. Second, the forest hardening calculation (Eq. (B3), Appendix B) assumes that the dislocation density is uniform within the matrix. As reported above, however, the density of punched dislocations is higher near the particle-rich regions. Glide of dislocations within the aluminum-rich, dislocation-poor regions may thus be easier.

The low yield stress of the fine-grained, extruded sample, exhibiting an average yield stress increase of $\Delta\sigma = 25$ MPa, is puzzling, since the particle distribution is improved (Fig. 3) and Hall–Petch strengthening (which was negligible for the coarse-grained, as-cast sample) gives a further contribution of $\sigma_2 = 61$ MPa (Eq. (B2), Appendix B). We note, however, that the Hall–Petch constant given in Appendix B was determined for the 0.2% proof stress and may be significantly smaller for the yield stress.

4.2.2. Continuum mechanics models

The shear-lag theory, as modified by Nardone and Prewo [34], predicts a single strengthening contribution $\Delta\sigma_c$ (for load transfer from the matrix to cylindrical particles of aspect ratio unity)

$$\Delta\sigma_c = \beta\sigma_0 V_p \quad (2)$$

where $\beta = 1/2$ and the yield stress of the annealed matrix (99.8% pure aluminum [26]) is $\sigma_0 = 20$ MPa. This approach has, however, been criticized for reinforcements with small aspect ratios [38]. More precise finite element calculations for β by Bao et al. [44] for the constrained flow of an elastic, perfectly plastic matrix containing spherical particles yield $\beta = 0.375$ for low volume fractions increasing to $\beta = 0.50$ for $V_p = 0.25$. These values are thus in reasonable agreement with the results given by the modified shear-lag theory for volume fractions below $V_p = 0.25$.

For ODS-Al with a volume fraction $V_p = 0.25$, Eq. (2) predicts $\Delta\sigma_c = 2.5$ MPa, significantly below the observed yield strength increase of 25–40 MPa. While particle clustering has been predicted to increase the value of the constant β [45], the discrepancy is too large to be explained by this effect.

It follows from the above discussion that continuum mechanics predictions for the yield stress, which ignore particle size effects, are significantly lower than the observed values for ODS-Al. This indicates that dislocation strengthening is operational, albeit to a lesser extent than predicted by Eqs. (B1)–(B3) (Appendix B), because of the inhomogeneous particle distribution in the matrix (Figs. 2 and 3). Fig. 6, showing a relaxed pile-up of straight, parallel dislocations blocked by alumina particles, illustrates that Orowan strengthening is probably operative.

4.3. Strain hardening in metals containing non-shearable particles

The strain hardening rate for both as-cast and extruded ODS-Al is high, leading to high values of the 0.2% proof stress (Table 1), despite the modest level of yield stress. In the following, we compare this behavior with that of other metallic systems containing non-shearable particles.

4.3.1. Metal matrix composites

In agreement with the behavior of ODS-Al, many investigators have observed high rates of strain hardening in MMCs containing particulates larger than 1 μm [46–49]. Corbin and Wilkinson [46] proposed a qualitative explanation for the high rate of strain hardening of Al–7Si–0.5Mg reinforced with 21 vol.% SiC particulates, 8 μm in diameter. Particle-free regions, which were as large as 50 μm in their composites, were assumed to yield at a low stress, harden rapidly and transfer load to the particle-rich regions, which remained elastic up to high stresses as a result of local constraints. The material thus exhibited a high apparent rate of strain hardening, followed by a rapid loss in hardening rate, as the particle-rich regions started to deform. Both the reinforced and unreinforced alloy exhibited similar rates of strain hardening at plastic strains above about 2×10^{-3}. Although, as discussed in the previous section, particle clustering may explain the low values of yield stress measured in ODS-Al, we do not believe that the above model can be applied to our materials for two reasons. First, the particle-poor regions in ODS-Al are about 1 μm in diameter and are thus much smaller than the 50 μm particle-free regions in the above MMC (the few aluminum-rich regions as large as 10 μm in ODS-Al are considered to be too rare to influence significantly the strain hardening rate). Second, the strain hardening rate of ODS-Al is significantly higher than that of pure aluminum up to fracture (strains between 0.05 and 0.1), much above the strain at which particle-free regions are expected to deform elastically (about 2×10^{-3}, as reported above). Below, we examine other models to explain the strain hardening behavior of ODS-Al.

4.3.2. Dispersion-strengthened metals

Unlike ODS-Al in the present study, mechanically alloyed aluminum with submicrometer grains containing large volume fractions of fine oxide and carbide dispersoids exhibits high yield stress values and very little work hardening up to about 1% deformation, above which work softening takes place [43]. The strength of these materials was modeled assuming boundary and dispersion strengthening (Eqs. (B1) and (B2), Appendix B), and the low strain hardening rate was interpreted as the result of a very high density of dislocations (on the order of the saturation value) in the as-fabricated samples, reorganizing themselves as the strain increases, similar to dynamic recovery.

Ashby [50,51] developed a model for metals containing dilute dispersions of submicrometer particles, whereby the strain hardening results from the interaction of primary glide dislocations, responsible for the overall deformation of the crystal, with secondary prismatic loops intersecting the glide plane of the primary dislocations. The prismatic loops are punched into the matrix as a result of the mismatch existing between the rigid inclusions and the plastically deformed matrix, and are thus geometrically necessary to prevent cavitation at the interface. Detailed nucleation mechanisms for these prismatic loops, involving double cross-slip of primary dislocations at the particle, have been reviewed by many workers [47,51–55]. The density ρ of these geometrically necessary prismatic loops is

$$\rho = \frac{3\sqrt{2}f\varepsilon_p}{\pi bd} \tag{3}$$

where f is the volume fraction of inclusions, ε_p is the plastic strain in the matrix and d is the particle diameter.

Introducing Eq. (3) into a forest hardening equation of the type given by Eq. (B3) (Appendix B), a parabolic strain hardening behavior is predicted

$$\sigma_p = \alpha' G\left(\frac{bf\varepsilon_p}{d}\right)^{1/2} \tag{4}$$

where α' is a constant on the order of 0.4 and G is the shear modulus of the matrix.

Brown and Stobbs [55] further considered the back stress due to these dislocations and derived another contribution of the form $\sigma_b = f^{1/2}\sigma_p$. Adding both contributions gives

$$\sigma'_p = \alpha' G(1 + f^{1/2})\left(\frac{bf\varepsilon_p}{d}\right)^{1/2} \tag{5}$$

Fig. 11 shows the stress as a function of the square root of the plastic strain for as-cast and extruded ODS-Al tested in tension at room temperature. The experimental curves exhibit a much higher initial strain hardening rate than predicted by Eq. (5), decreasing rapidly with strain to values comparable with Eq. (5) at strains of about 0.04. We believe that the comparison between our as-cast ODS-Al material and the above model, developed for single-crystal materials, is appropriate, because as-cast ODS-Al exhibits very coarse grains in the centimeter range. The orientation of the few strained grains with respect to the applied stress is unknown, but this uncertainty brings an error factor of about two with respect to Eq. (5). The much higher initial strain hardening rate (about a factor of ten in the slope in Fig. 11), however, clearly indicates a discrepancy with the above model, as does the rapidly decreasing strain hardening.

4.4. Modeling of strain hardening in ODS-Al

In this section, a simple extension of Ashby's model [51,53] is presented to explain the strain hardening behavior of ODS-Al. We assume that the basic assumption of Ashby's model, i.e. interaction of primary glide dislocations with secondary dislocations produced by the particles, can be applied to the present system, since both types of dislocations are observed in the deformed samples (Figs. 5 and 6). First, we explain the high initial strain hardening rate by assuming a density of secondary punched dislocation loops much higher than predicted by Ashby's model. Second, we justify the rapid decrease in strain hardening with increasing strain by considering the recovery of these secondary dislocations by mutual annihilation.

4.4.1. Initial rate of strain hardening

We assume that the high initial rate of strain hardening is due to a density of secondary dislocations higher than that predicted by Eq. (3) (Appendix B), leading to increased interaction with the primary glide disloca-

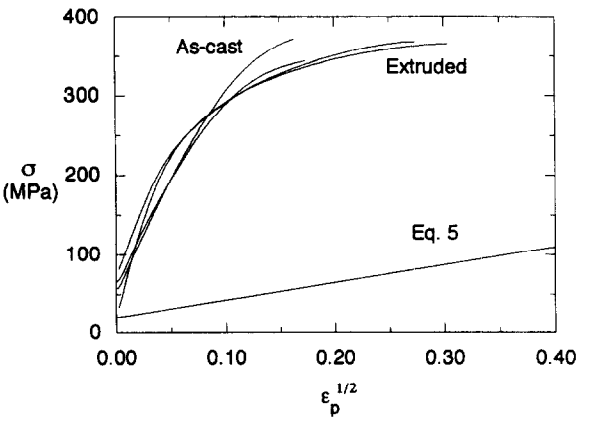

Fig. 11. True stress–plastic strain curve for ODS-Al in the as-cast and extruded (550 °C) conditions. The line is the predicted behavior according to Eq. (5), with a yield stress of 20 MPa.

tions. Two possible mechanisms can be proposed for an increased density of secondary dislocations, both of which rely on the larger size of the particles compared with the small dispersoids considered in Ashby's model. First, the matrix already contains dislocations before deformation as a result of the punching of prismatic loops due to the thermal mismatch on cooling (Fig. 4), the density of which is given by Eq. (B4) (Appendix B). These dislocations are only expected to be punched by particles with a diameter above the critical value d^* (Eq. (1)), and were therefore not considered in Ashby's model, which describes particles with diameters below this threshold. Entanglement is expected on interaction between these prismatic loops punched by thermal mismatch (which are of interstitial character and are expected to be punched along all glide directions) and the prismatic loops punched by deformation mismatch (which are both interstitial and vacancy in character and are punched preferentially along the directions of maximum strain mismatch). As a result of entanglement between these loops, dislocation multiplication can take place and the total density of secondary dislocations is above that given in Eq. (3), with the result that the initial strain hardening is higher (Eq. (4)). Entanglement has also been observed around large particles punching prismatic loops on CTE mismatch [56,57] or bulk modulus mismatch [58]. The above hypothesis is also supported indirectly by the observation of Humphreys [38], who reported that unalloyed aluminum containing 17 vol.% SiC particles, 3 μm in diameter, exhibits greater rates of strain hardening after quenching than after furnace cooling; on quenching, the rate of dislocation punching is much higher, and thus the probability of entanglement leading to dislocation multiplication is increased.

Another possible explanation for an increased secondary prismatic loop density also takes into account the large size of the particles. In Ashby's model [51,53], the diameter of the prismatic loops is assumed to be comparable with that of the particles, since the prismatic loops form by cross-slip of the screw components of a shear loop along the cylinder of maximum shear stress [52,59]. This assumption is justified by numerous TEM observations of deformed metals containing small dispersoids [51,58,59]. However, as the particle diameter increases, the probability increases that the screw components will encounter an obstacle before completing a loop of maximum radius r, interrupting the process and leading to a smaller loop. The net result is that a single large loop of radius r is replaced by numerous prismatic loops with a smaller radius r', but a larger total length than the single prismatic loop of radius r. Assuming that the total area of loops is constant, the secondary prismatic loop density is then

$$\rho' = \rho \frac{r}{r'} \tag{6}$$

Furthermore, an increased dislocation density is expected if the particle exhibits stress concentrators, such as sharp corners, which also punch loops of smaller diameters [57]. Indeed, Fig. 5 shows that the dislocations found around the particles are significantly smaller than the particle diameter.

Although the observed increase in the slope $\sigma_p/\varepsilon_p^{1/2}$ by a factor of about ten for ODS-Al is high (Fig. 11), it is plausible: it corresponds to an increase in the punched dislocation length by a factor of about 100 (i.e. a decrease in the average loop diameter by the same factor, Eq. (6)) or an increase in the dislocation density by entanglement by a factor of 100, or a combination of these mechanisms.

4.4.2. Strain dependence of strain hardening

We assign the steep decrease in strain hardening with increasing strain to the recovery of secondary dislocation loops, as also reported by Ashby [51,53]. One mechanism for dislocation recovery discussed by Ashby is cavitation. Cavitation is expected to occur at decreasing strains, as the size of the particle increases, and may thus be responsible for the observed decrease in strain hardening in ODS-Al. However, no evidence of cavitation was found during TEM observation of ODS-Al, indicating that this effect is probably negligible. Ashby also considered the recovery of pairs of prismatic loops of interstitial and vacancy nature, punched on opposite sides of a particle: the diffusion of atoms or vacancies leads to the annihilation of the pair. The rate of this recovery mechanism decreases with increasing diffusion distance and thus with increasing particle diameter. The strain rate $\dot{\gamma}$ at which recovery by annihilation and generation by punching are equal is [51]

$$\dot{\gamma} = \frac{2Db}{kT} \frac{G\Omega}{d^3} \tag{7}$$

where D is the diffusion coefficient, Ω is the atomic volume, k is Boltzmann's constant and T is the temperature. Using material values for aluminum given by Frost and Ashby [41], Eq. (7) predicts a critical strain rate of about 2×10^{-17} s^{-1}, i.e. much smaller than the experimental strain rate of 8×10^{-4}. We conclude that recovery by diffusion around particles with a diameter of 0.28 μm is negligible in aluminum at room temperature.

Instead, we propose a different recovery mechanism, also based on the annihilation of prismatic loops of opposite sign. Whereas Ashby [51,53] considered the interaction of loops of opposite sign on opposite sides of the same particle, annihilating each other by diffusional mass transport, we consider the annihilation of prismatic loops of opposite sign from neighboring par-

ticles, gliding towards each other. We note that the ratio of the loop diameter to the interparticle distance is assumed to be small in Ashby's model [51,53], which is applicable for dilute dispersions of small particles (diameter below 100 nm). Since the total length of a prismatic loop train decreases with decreasing loop diameter [60], annihilation by glide is only expected at very high strains in such systems, and is thus not discussed by Ashby [51,53]. However, in the case of ODS-Al containing large volume fractions of large particles, the dispersoid separation ($L = 0.18$ μm) is smaller than the particle diameter ($d = 0.28$ μm), and interaction between loop trains from neighboring particles is expected to take place at lower strains, especially since, for a given matrix strain, the number of loops in each pile-up (and thus the length of the pile-up) increases with the diameter of the inclusion. We thus expect that annihilation between loop trains of neighboring particles will take place at low strain, explaining the early departure from the constant slope in Fig. 11. Furthermore, the annihilation rate is expected to increase gradually with increasing strain, until it matches the generation rate of prismatic loops at the mismatching particles, as described below.

We assume that the shear strain around a particle is uniform (Fig. 12(a)): typical slip line spacing in dispersion-strengthened alloys is on the order of several tens of nanometers [47], much smaller than the particle size of 280 nm in ODS-Al. The volume mismatch between the rigid particle and the plastic matrix is not uniform for a uniform shear (Fig. 12(a)). The train of loops necessary to cancel this mismatch is formed of prismatic loops with decreasing diameter, if we take Ashby's assumption of a single pile-up [51,53]. Alternatively, if we assume that the volume mismatch is accommodated by multiple pile-ups of smaller prismatic loops, these pile-ups have varying numbers of loops, and thus varying total length, as shown in Fig. 12(b). In both cases, which are essentially equivalent, the projected diameter of the envelope containing the secondary prismatic loops (i.e. the plastic zone) decreases with increasing distance from the particle. Considering the interactions of such plastic zones between adjacent particles, it is apparent from Fig. 12 that the interaction volume increases gradually with strain. Since annihilation takes place within the interaction volume, because the signs of the dislocations are opposite in overlapping plastic zones, the annihilation rate increases with strain, until it matches the nucleation rate at the particles. The strain hardening thus decreases gradually with increasing strain, as also observed experimentally (Fig. 11).

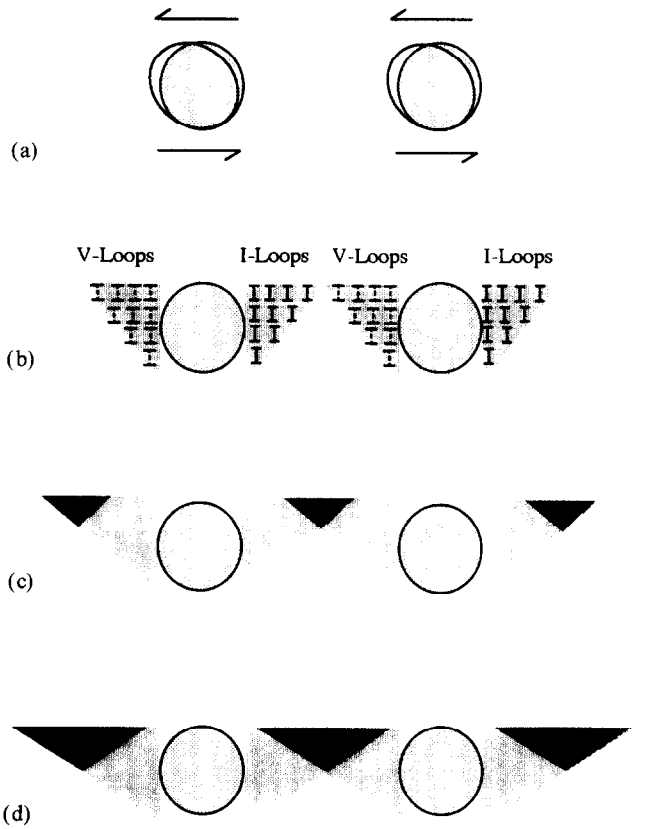

Fig. 12. Schematic diagram of prismatic loop annihilation on shear of a matrix containing a high volume fraction of rigid particles. (a) Elastic incompatibility between rigid particles and the homogeneously strained plastic matrix. (b) Trains of punched interstitial (I) and vacancy (V) prismatic loops, which are geometrically necessary to prevent cavitation at the particle interface. The envelope around the dislocations represents the plastic zone. (c), (d) As the strain increases, the size of the geometrically necessary plastic zone increases. Prismatic loops of opposite sign overlap in the shaded volume where they annihilate, decreasing the dislocation density and the rate of strain hardening.

4.4.3. Comparison with data

The above mechanisms qualitatively explain the observed high initial rate of strain hardening and its monotonic decrease with increasing strain observed in ODS-Al (Fig. 11). We do not attempt to quantify the above model, since it would require many assumptions concerning the effective friction stress of trains of loops through the tangles, the entanglement rate, the geometry of the trains punched by the particles, the particle size distribution, the geometric distribution of particles, etc. Although the above parameters influence the quantitative predictions of the models, they do not invalidate the qualitative features listed above. Furthermore, it is apparent from Figs. 6 and 7 that the actual dislocation structure in ODS-Al is much more complex than the idealized structure shown in Fig. 12(b). Again, we believe that the two qualitative predictions made above are not influenced by the actual dislocation arrangement, as long as initial entanglement and progressive annihilation between dislocations of opposite sign take place.

As seen in Fig. 11, the strain hardening behavior of extruded, fine-grained ODS-Al is not significantly different from that of as-cast, coarse-grained ODS-Al. Grain boundaries are obstacles for the motion of primary glide dislocations and thus may affect the yield strength (Eq. (B2), Appendix B). The strengthening contribution of grain boundaries is, however, constant with strain, and is thus not expected to influence the strain hardening. A possible indirect contribution, which may vary with strain, consists of dislocations produced as a result of strain incompatibilities between adjacent grains. This contribution seems, however, to be negligible in the case of ODS-Al. Finally, we note that the dislocation structure of as-cast ODS-Al is quite different from that of extruded ODS-Al: unlike the latter samples, a well-developed subgrain structure is observed in the former samples. This may be explained by the fact that the grain size of the extruded samples is on the order of the subgrain size found in deformed aluminum [61] and thus subgrain formation is inhibited.

4.5. Fracture

The measured fracture toughness of as-cast ODS-Al ($K_{1C} = 18$ MPa $m^{1/2}$) is similar to that of cast or extruded aluminum matrix composites with comparable volume fractions of reinforcement [31]. The ductility of extruded ODS-Al (9.4%–11%, Table 1) is also comparable with that reported by Humphreys et al. [28] for extruded pure aluminum with 25 vol.% SiC fabricated by powder metallurgy: these workers found ductilities of 13% for particles sizes of 3, 7 and 20 μm, decreasing to 8% for 40 μm particles and 5% for 100 μm particles. The lower ductility values found in the as-cast ODS-Al (4.7%, Table 1) is probably the result of the higher extent of particle clustering (Fig. 2): regions with locally higher volume fractions of reinforcement exhibit a lower ductility and control the overall ductility of the composite [62]. The large spread of values (varying between 3.2% and 6%) can be attributed, at least in one instance, to a large (1 mm) solidification defect which initiated premature failure, suggesting that the ductility of the as-cast materials is sensitive to particle distribution and processing conditions. Subsequent extrusion leads to improved particle distribution and reduction of these casting inhomogeneities.

The microdimples observed on both the as-cast and extruded fracture surfaces (Fig. 7(b)) are typical for dispersion-strengthened materials, and suggest that fracture occurs by nucleation and growth of voids at particles, and by plastic deformation of the elongated ridges at the rim of the dimples [63]. On a larger scale, the zig-zag fracture path, observed in extruded ODS-Al, has also been found in aluminum alloys (but not in pure aluminum) [64,65], copper [66], maraging steels [67] and titanium and cobalt alloys [64]. The peak-to-peak spacing (50–100 μm) of the zig-zag front of our material is within the range reported for the materials above, i.e. from 10 μm [68] to 800 μm [67]. According to Van Den Avyle [65], the features common to all these materials are: (i) the presence of 0.05–0.5 μm second-phase particles with a spacing-to-diameter ratio on the order of 10 to 1; (ii) fracture by microvoid initiation, growth and coalescence on ridges; (iii) moderate to high fracture toughness of the alloy; (iv) a high degree of triaxiality ahead of the crack tip; (v) plane strain conditions ahead of the crack tip. Features (i)–(iii) are indeed observed in ODS-Al.

To explain zig-zag fracture, McClintock [69] proposed a combined Mode I–Mode II fracture criterion which predicts crack propagation along the line separating the regions of high hydrostatic stress (in front of the crack tip) and high shear strain (above and below the crack front). These predictions are made for a non-propagating sharp crack in a non-hardening material: strain hardening increases the stress concentration in the near-tip region and crack tip blunting affects both the spacing and the angle of the zig-zag path. Since strain hardening is very low when the ODS-Al samples fracture (Fig. 11), the non-hardening case can be applied. The zig-zag crack is then proposed to propagate in the following sequence [65]: (i) the crack begins to grow within the macroscopic plastic zone at a 45° angle to the macroscopic crack plane, following a line of constant hydrostatic stress; (ii) when the crack reaches a point where the combined critical hydrostatic stress/shear strain criterion is lower along the 45° path than the competing strain field of another perpendicular slip line also 45° to the macroscopic plane, the crack changes direction and moves towards the macroscopic crack plane; (iii) the crack follows this slip line until the process is repeated.

4.6. High-temperature strength

Fig. 9 shows that the proof and ultimate stresses for the ODS materials decrease linearly with temperature between 20 and 260 °C, and that solid solution strengthening of the matrix improves the elevated temperature strength. A similar decrease was found for unalloyed aluminum MMCs with 20 vol.% SiC particles tested in compression [70]; furthermore, the flow stress was found to decrease at all temperatures with increasing particle size (1, 3 and 20 μm). This is expected for MMCs with large particles, since most of their strength is derived from dislocation punching (Eq. (B4), Appendix B): the strength is expected to decrease rapidly at elevated temperature, due to matrix creep (reducing the matrix yield stress) and dislocation annealing (as a result of recovery and recrystallization). However, in aluminum containing smaller dispersoids, for which dispersion strengthening (Eq. (B1), Appendix B) and

boundary strengthening (Eq. (B2), Appendix B) become important, the strengthening mechanisms are still operative at elevated temperature for dislocation-glide-controlled flow, albeit to a lesser extent than at low temperature, due to diffusion and climb processes [71,72] and a decrease in elastic modulus. As shown by the annealing experiments, the fine grain size of extruded ODS-Al is exceptionally stable, since only a slight increase in grain size was found after annealing for 139 h at a homologous temperature of 0.99. A decrease in reinforcement size is thus expected to bring a higher strength at elevated temperature due to boundary strengthening, provided that grain boundary sliding is inhibited by the high volume fraction of particles, as observed in many mechanically alloyed aluminum alloys and SAP [7,73,74] materials.

Fig. 8 shows that the hardness also decreases with temperature. However, ODS-Al is harder than the precipitation-strengthened alloy 6061 at all temperatures, especially above about 225 °C, where precipitate dissolution and coarsening take place in Al-6061. Compared with the hardness values of the rapidly solidified, high-temperature alloy AA-8009 (Al–8Fe–1V–1.2Si), unalloyed ODS-Al is softer, but shows a similar temperature dependence. The data shown in Fig. 8 suggest that ODS-Al retains useful strength values up to 450 °C. For example, at 465 °C (corresponding to a homologous temperature of 0.79), the hardness of ODS-Al is HV = 173 MPa, which, using the conversion HV = 3UTS, corresponds to an ultimate tensile strength (UTS) value of 58 MPa. This conversion is found to hold reasonably well for the UTS values of extruded ODS-Al measured at lower temperatures (Table 1), as shown by the converted UTS values plotted as open symbols in Fig. 8.

5. Conclusions

(1) Binder-free preforms with 0.1–0.4 μm α-alumina particles were pressure infiltrated with liquid aluminum (99.9% Al or Al–2.5%Mg), resulting in pore-free ODS-Al containing 25 vol.% alumina particles, which are neither sintered nor coarsened. The particle size is smaller than that of most MMCs, but larger than that of typical precipitation-hardened, rapidly solidified or mechanically alloyed aluminum alloys.

(2) The grain size of ODS-Al can vary from millimeters in the as-cast condition to micrometers in the extruded, recrystallized condition. Grain growth is negligible at temperatures as high as 650 °C.

(3) The Young's modulus of ODS-AlMg is 110 GPa, as predicted from continuum mechanics models assuming elastic stress transfer without interfacial debonding.

(4) The room temperature yield stress is low (on the order of 60 MPa), but high strain hardening rates lead to high values of the 0.2% proof stress (170 MPa and 215 MPa) and ultimate tensile strength (330 and 340 MPa) for as-cast and extruded ODS-Al respectively. The room temperature ductilities are 5% and 10% respectively. Matrix alloying improves the strength but decreases the ductility.

(5) The initial strain hardening of ODS-Al is much higher than that predicted by Ashby's model [51,53], developed for small volume fractions of small dispersoids, whereby primary glide dislocations interact with secondary prismatic loops punched by the particles as a result of strain mismatch. Two additional mechanisms are proposed within the framework of Ashby's model, taking into account the large particle size representative of ODS-Al: entanglement of the primary dislocations with (i) prismatic loops produced by thermal mismatch or (ii) prismatic loops produced by strain mismatch, with a diameter smaller, and thus a density larger, than those considered by Ashby. For both mechanisms, the interaction with glide dislocations is enhanced, thus explaining the high initial strain hardening observed in ODS-Al.

(6) The strain hardening of ODS-Al decreases rapidly with increasing strain. The interaction of prismatic loops punched from adjacent particles is proposed as a relaxation mechanism. Since the loops are of opposite sign in adjacent plastic zones, they annihilate with increasing frequency as the overlap between the plastic zones increases with strain. This assumption stems from the small interparticle distance compared with the particle diameter, i.e. from the large volume fraction of particles.

(7) The strength of ODS-Al decreases with increasing temperature from 20 to 260 °C. The hardness data suggest that strength values on the order of 60 MPa are retained at temperatures up to 460 °C, as a result of dispersion strengthening.

Acknowledgments

A.M.B. and E.M.K. acknowledge support from the National Science Foundation (NSF) in the form of a Small Business Innovation Research (SBIR) grant (ISI 91-60518) to Chesapeake Composites Corporation. A.M.R. and D.C.D. acknowledge the support of the Department of Defence (DOD) (in the form of a National Defense Science and Engineering Graduate (NDSEG fellowship) and AMAX (in the form of an endowed chair at the Massachusetts Institute of Technology (MIT)) respectively. The authors are grateful to Dr. W. Hunt (Alcoa) for room temperature mechanical testing and optical microscopy of the as-cast material

and Dr. R. Wills (TRW) and Dr. M. Zedalis (Allied Signal) for elevated temperature tensile testing of extruded ODS-Al and ODS-AlMg respectively.

Appendix A: Elastic modulus calculations

Fig. 10 shows a plot of the elastic modulus of Al/Al_2O_3 composites as a function of the volume fraction of alumina V_r, according to the three models described below. The material constants used to plot Eqs. (A1), (A2) and (A6) in Fig. 10 are: $E_m = 70.3$ GPa and $\nu_m = 0.345$ [75], $E_r = 350$ GPa and $\nu_r = 0.23$ [42,76].

Shear-lag theory

For the case where stress transfer occurs both along the sides and at the ends of cylindrical fibers of aspect ratio unity, the shear lag theory gives [12]

$$E_{SL} = E_{ROM} - V_r(E_r - E_m)\tanh\left(\sqrt{-\frac{6G_m}{E_r \ln V_r}}\right) \times \sqrt{-\frac{E_r \ln V_r}{6G_m}} \quad \text{(A1)}$$

where $E_{ROM} = (1 - V_r)E_m + V_r E_r$ is the elastic modulus predicted by the rule of mixtures, G_m is the shear modulus of the matrix and it is assumed that $V_r = (d/\delta)^3$, where δ is the diameter of the unit cell and d is the fiber diameter.

Halpin–Tsai equation

For fibers of unit aspect ratio, the Halpin–Tsai equation is [34]

$$E_{HT} = E_m \frac{1 + nV_r(2 + 40V_r^{10})}{1 - nV_r} \quad \text{(A2)}$$

where

$$n = \frac{E_r - E_m}{E_r + E_m(2 + 40V_r^{10})} \quad \text{(A3)}$$

Self-consistent variation method

Hashin and Shtrikman [33] derived bounds for the composite shear modulus G^* and bulk modulus K^*

$$G^* = G_i + V_j\left[\frac{1}{G_j - G_i} + \frac{6V_i(K_i + 2G_i)}{5G_i(3K_i + 4G_i)}\right]^{-1} \quad \text{(A4)}$$

$$K^* = K_i + V_j\left(\frac{1}{K_j - K_i} + \frac{3V_i}{3K_i + 4G_i}\right)^{-1} \quad \text{(A5)}$$

where G and K are the shear modulus and bulk modulus respectively of phase i or j. Using the subscripts $i = m$ and $j = r$ in Eqs. (A4) and (A5) gives the lower bounds for the elastic constants, while $i = r$ and $j = m$ gives the upper bounds. The bounds for the elastic modulus E_{HS} are calculated by introducing Eqs. (A4) and (A5) with the appropriate subscripts into

$$E_{HS} = \frac{9K^*G^*}{3K^* + G^*} \quad \text{(A6)}$$

Appendix B: Strengthening mechanisms

From a dislocation micromechanism viewpoint, the yield strength of a pure metal containing a second phase is determined by the interaction of primary glide dislocations with (i) the second phase, (ii) grain and subgrain boundaries and (iii) other dislocations. Following Refs. [14,28,38], the respective contributions of these three mechanisms at room temperature are discussed below.

Assuming that glide dislocations interact with particles by bowing around them (mechanism (i)), the increase in yield strength σ_1 due to dislocation bypass of spherical dispersoids, separated by a distance L, is given by the Orowan equation [77]

$$\sigma_1 = M\frac{0.4Gb}{\pi L}\frac{\ln(\bar{d}/b)}{\sqrt{1 - \nu}} \quad \text{(B1)}$$

where $G = 23.4$ GPa, $\nu = 0.345$ and $b = 0.286$ nm are the single-crystal shear modulus, Poisson's ratio and Burger's vector of pure aluminum respectively, $M = 3.06$ is the mean orientation factor for f.c.c. metals [75] and $\bar{d} = (2/3)^{1/2}d$ is the mean diameter of a circular section in a random plane for a sphere of diameter d. For a cubic arrangement of spherical dispersoids of volume fraction V_p, the dispersoid separation is $L = d[(\pi/4V_p)^{1/2} - 1]$ [77].

Strengthening by grain boundaries (mechanism (ii)) is given by the Hall–Petch relationship

$$\sigma_2 = KD^{-1/2} \quad \text{(B2)}$$

where D is the grain size and K is the Hall–Petch constant, measured as $K = 0.06$ MPa $m^{1/2}$ by Frazier and Koczak [13] for pure aluminum with grain sizes between 0.3 and 2 μm, i.e. near the range of particle size and fractions of interest in the present study. In the same grain size range, Sahoo and Lund [78] found $K = 0.085$ MPa $m^{1/2}$. We use the average value $K = 0.0725$ MPa $m^{1/2}$. Smaller values of K have been measured for larger grain sizes [79,80].

Geometrically necessary dislocations, resulting from the relaxation of thermal expansion mismatch between the matrix and the second phase, also contribute to strengthening (mechanism (iii)) [35,37,81–83]

$$\sigma_3 = AGb\rho_{th}^{1/2} \quad \text{(B3)}$$

where A is a constant equal to 1.25 for aluminum [79] and ρ_{th} is the density of dislocation loops of radius

$d/\sqrt{2}$ punched by spherical particles of diameter d, assuming full relaxation of the mismatch due to the difference in thermal expansion coefficients $\Delta\alpha$ for a temperature excursion ΔT [40]

$$\rho_{th} = \frac{12\sqrt{2}\Delta\alpha\Delta T V_p}{bd(1-V_p)} \quad \text{(B4)}$$

For the system Al/Al_2O_3, we take $\Delta\alpha = 1.5 \times 10^{-5}$ K^{-1} and $\Delta T = 250$ K. The latter parameter is chosen so that the upper temperature at which dislocation punching is assumed to begin is $T_{max} = 550$ K, corresponding to a homologous temperature of 0.59. Above T_{max}, all mismatch is assumed to be relaxed by diffusion, as also observed for quenched AgCl containing glass spheres at homologous temperatures of 0.55 ± 0.04 [40].

For the experimental parameters $V_f = 0.25$, $d = 0.28$ μm and $D = 1.4$ μm (for the sample extruded at 550 °C) or $D = 1$ cm (for the as-cast samples), the three strengthening mechanisms described above are: $\sigma_1 = 121$ MPa (Orowan strengthening, Eq. (B1)), $\sigma_2 = 61$ MPa for the extruded sample and $\sigma_2 = 1$ MPa for the as-cast sample (Hall–Petch strengthening, Eq. (B2)) and $\sigma_3 = 136$ MPa (forest strengthening, Eqs. (B3) and (B4)).

References

[1] C.R. Brooks, *Heat Treatment, Structure and Properties of Nonferrous Alloys*, American Society for Metals, Metals Park, OH, 1982, pp. 115–1374.

[2] I.J. Polmear, *Light Alloys: Metallurgy of the Light Metals*, Edward Arnold, London, 1989, pp. 18–168.

[3] J.M. Sater, S.C. Jha and T.H. Sanders, Jr., in A.K. Vaseduvan and R.D. Doherty (eds.), *Aluminum Alloys—Contemporary Research and Applications*, Academic Press, Boston, MA, 1989, pp. 409–444.

[4] F.H. Froes, Y.-W. Kim, S. Krishnamurthy and R. Sundaresan, in I. Jenkins and J.V. Wood (eds.), *Powder Metallurgy: an Overview*, The Institute of Metals, London, 1991, pp. 220–255.

[5] W.M. Doyle, *Sheet Met. Ind.*, *32* (1955) 889.

[6] E.A. Bloch, *Metall. Rev.*, *6* (1961) 193.

[7] N. Hansen, *Powder Metall.*, *10* (1967) 95.

[8] J.S. Benjamin and M.J. Bomford, *Metall. Trans. A*, *8* (1977) 1301.

[9] V. Arnhold and J. Baumgarten, *Powder Metall. Int.*, *17* (1985) 168.

[10] J.H. Weber and R.D. Schelleng, in Y.-W. Kim and W.M. Griffith (eds.), *Dispersion Strengthened Aluminum Alloys*, TMS, Warrendale, PA, 1988, pp. 467–482.

[11] R. Sundaresan and F.H. Froes, in E. Arzt and L. Schultz (eds.), *New Materials by Mechanical Alloying Techniques*, DGM Verlag, Oberursel, 1989, pp. 243–263.

[12] M. Taya and R.J. Arsenault, *Metal Matrix Composites: Thermomechanical Behavior*, Pergamon, Oxford, 1989, pp. 49–112.

[13] W.E. Frazier and M.J. Koczak, in Y.-W. Kim and W.M. Griffith (eds.), *Dispersion Strengthened Aluminum Alloys*, TMS, Warrendale, PA, 1988, pp. 573–602.

[14] W.S. Miller and F.J. Humphreys, *Scr. Metall. Mater.*, *25* (1991) 33.

[15] D.C. Dunand and B. Derby, in S. Suresh, A. Mortensen and A. Needleman (eds.), *Fundamentals of Metal Matrix Composites*, Butterworth-Heinemann, Boston, MA, 1993, pp. 191–214.

[16] A.L. Geiger and J.A. Walker, *J. Met.*, *43* (1991) 8.

[17] M.J. Tan, L.H. Koh, K.A. Khor, F.Y.C. Boey, Y. Murakoshi and T. Sano, *J. Mater. Process Technol.*, *37* (1993) 391.

[18] R.J. Arsenault, *J. Compos. Tech. Res.*, *10* (1988) 140–145.

[19] S.J. Hong, P.W. Kao and C.P. Chang, *Mater. Sci. Eng. A*, *158* (1992) 195.

[20] H.C. Yi, A. Petric and W.W. Smeltzer, in V.A. Ravi, T.S. Srivatsan and J.J. Moore (eds.), *Processing and Fabrication of Advanced Materials*, Vol. III, TMS, Warrendale, PA, 1994, pp. 763–769.

[21] R.M. Aikin, Jr. and L. Christodoulou, *Scr. Metall. Mater.*, *25* (1991) 9.

[22] K. Shanker, R.A.L. Drew, L.T. Mavropoulos and P.G. Tsantrizos, *Composites*, *23* (1992) 47.

[23] D. Muscat, K. Shanker and R.A.L. Drew, *Mater. Sci. Technol.*, *8* (1992) 971.

[24] J.E. Allison and G.S. Cole, *J. Met.*, *45* (1993) 19.

[25] A. Mortensen and I. Jin, *Int. Mater. Rev.*, *37* (1992) 101–128.

[26] J.E. Hatch, *Aluminum: Properties and Physical Metallurgy*, American Society for Metals, Metals Park, OH, 1984, p. 855.

[27] W.H. Cubberly et al. (eds.), *Metals Handbook: Properties and Selection: Nonferrous Alloys and Pure Metals*, American Society for Metals, Metals Park, OH, 1979.

[28] F.J. Humphreys, A. Basu and M.R. Djazeb, in D. Juul-Jensen. N. Hansen, T. Leffers, H. Lilholt, T. Lorentzen, A.S. Pedersen, O.B. Pedersen and B. Ralph (eds.), *Metal Matrix Composites—Processing, Microstructure and Properties*, Risø National Laboratory, Roskilde, Denmark, 1991, pp. 51–66.

[29] D.Y. Lee and D.E. Zupon, in Y.-W. Kim and W.M. Griffith (eds.), *Dispersion Strengthened Aluminum Alloys*, TMS, Warrendale, PA, 1988, pp. 265–281.

[30] D.J. Skinner, in Y.-W. Kim and W.M. Griffith (eds.), *Dispersion Strengthened Aluminum Alloys*, TMS, Warrendale, PA, 1988, pp. 181–197.

[31] A. Mortensen, *Fabrication of Particulate Reinforced Metal Composites*, ASM International, Metals Park, OH, 1990, pp. 217–233.

[32] H.J. Seemann, *Metallurgy*, *17* (1963) 997.

[33] Z. Hashin and S. Shtrikman, *J. Mech. Phys. Solids*, *11* (1963) 127.

[34] V.C. Nardone and K.M. Prewo, *Scr. Metall.*, *20* (1986) 43.

[35] D. Dew-Hughes, *Acta Metall.*, *8* (1960) 816.

[36] R.J. Arsenault, *Mater. Sci. Eng.*, *64* (1984) 171.

[37] B. Derby and J.R. Walker, *Scr. Metall.*, *22* (1988) 529.

[38] F.J. Humphreys, in S.I. Andersen, H. Lilholt and O.B. Pedersen (eds.), *Mechanical and Physical Behavior of Metallic and Ceramic Composites: 9th Risø International Symposium on Metallurgy and Materials Science*, Risø National Laboratory, Roskilde, Denmark, 1988, pp. 51–74.

[39] P.M. Hazzledine, *Scr. Metall. Mater.*, *26* (1992) 57.

[40] D.C. Dunand and A. Mortensen, *Acta Metall. Mater.*, *39* (1991) 127.

[41] H.J. Frost and M.F. Ashby, *Deformation-Mechanism Maps: The Plasticity and Creep of Metals and Ceramics*, Pergamon, Oxford, 1982, p. 166.

[42] J. Shackelford and W. Alexander (eds.), *The CRC Materials Science and Engineering Handbook*, CRC Press, Boca Raton, FL, 1992.

[43] J.A. Hawk and H.G.F. Wilsdorf, in J.B. Bilde-Sorensen (ed.), *Materials Architecture: Proceedings of the 10th Risø International Symposium on Metallurgy and Materials Science*, Risø National Laboratory, Roskilde, Denmark, 1989, pp. 371–376.

[44] G. Bao, J.W. Hutchinson and R.M. McMeeking, *Acta Metall. Mater.*, *39* (1991) 1871.

[45] J.W. Hutchinson and R.M. McMeeking, in S. Suresh, A. Mortensen and A. Needleman (eds.), *Fundamentals of Metal*

Matrix Composites, Butterworth-Heinemann, Boston, MA, 1993, pp. 158–173.
[46] S.F. Corbin and D.S. Wilkinson, in N. Hansen, D. Juul-Jensen, T. Leffers, H. Lilholt, T. Lorentzen, A.S. Pedersen, O.B. Pedersen and B. Ralph (eds.), *Metal Matrix Composites—Processing, Microstructure and Properties*, Risø National Laboratory, Roskilde, Denmark, 1991, pp. 283–290.
[47] F.J. Humphreys, *Dislocations and Properties of Real Materials*, The Institute of Metals, London, 1985, pp. 175–204.
[48] S.V. Kamat, A.D. Rollett and J.P. Hirth, *Scr. Metall. Mater.*, *25* (1991) 27.
[49] J.J. Lewandowski, D.S. Liu and C. Liu, *Scr. Metall. Mater.*, *25* (1991) 21.
[50] M.F. Ashby, *Philos. Mag.*, *21* (1970) 399.
[51] M.F. Ashby, in A. Kelly and R.B. Nicholson (eds.), *Strengthening Methods in Crystals*, Applied Science Publishers, London, 1970, pp. 137–192.
[52] P.B. Hirsch, *J. Inst. Met.*, *86* (1957) 7.
[53] M.F. Ashby, *Second International Conference on the Strength of Metals and Alloys, Pacific Grove, California*, American Society for Metals, Metals Park, OH, 1970, pp. 507–541.
[54] L.M. Brown and W.M. Stobbs, *Philos. Mag.*, *23* (1971) 1185.
[55] L.M. Brown and W.M. Stobbs, *Philos. Mag.*, *23* (1971) 1201.
[56] D.C. Dunand and A. Mortensen, *Scr. Metall. Mater.*, *25* (1991) 761.
[57] D.C. Dunand and A. Mortensen, *Mater. Sci. Eng. A*, *135* (1991) 179.
[58] M.F. Ashby, S.H. Gelles and L.E. Tanner, *Philos. Mag.*, *19* (1969) 757.
[59] F.J. Humphreys and P.B. Hirsch, *Proc. R. Soc. London, Ser. A*, *318* (1970) 73.
[60] D.C. Dunand and A. Mortensen, *Scr. Metall. Mater.*, *25* (1991) 607.
[61] H.J. McQueen and J.E. Hockett, *Metall. Trans.*, *1* (1970) 2997.
[62] J.D. Embury, *Metall. Trans. A*, *16* (1985) 2191.
[63] *Metals Handbook: Fractography*, American Society for Metals, Metals Park, OH, 1987.
[64] J.W. Carson, K. Mills et al. (eds.), *Ph.D. Thesis*, Massachusetts Institute of Technology, Cambridge, MA, 1970.
[65] J.A. Van Den Avyle, K. Mills et al. (eds.),*Ph.D. Thesis*, Massachusetts Institute of Technology, Cambridge, MA, 1975.
[66] H.C. Rogers, *Trans. AIME*, *218* (1960) 498.
[67] G.R. Yoder, *Metall. Trans.*, *3* (1972) 1851.
[68] C.A. Berg, in M.F. Kanninen (ed.), *Inelastic Behavior of Solids*, McGraw-Hill, New York, 1970.
[69] F.A. McClintock, in A.S. Argon (ed.), *Physics of Strength and Plasticity*, MIT Press, Cambridge, MA, 1969, pp. 307–326.
[70] F.J. Humphreys, *Mater. Sci. Eng. A*, *135* (1991) 267.
[71] W. Blum and B. Reppich, *Creep Behavior of Crystalline Solids*, Pineridge Press, Swansea, 1985, p. 83.
[72] E. Arzt, in S. Ochiai (ed.), *Mechanical Properties of Metallic Composites*, Dekker, New York, 1994, pp. 205–223.
[73] W.C. Oliver and W.D. Nix, *Acta Metall.*, *30* (1982) 1335.
[74] J. Rösler, R. Joos and E. Arzt, *Metall. Trans. A*, *23* (1992) 1521.
[75] M.A. Meyers and K.K. Chawla, *Mechanical Metallurgy: Principles and Applications*, Prentice-Hall, Englewood Cliffs, NJ, 1984.
[76] J.W. Soh and H.M. Lee, *Scr. Metall. Mater.*, *27* (1992) 783.
[77] L.M. Brown and R.K. Ham, in A. Kelly and R.B. Nicholson (eds.), *Strengthening Methods in Crystals*, Elsevier, Amsterdam, 1971, pp. 9–135.
[78] M. Sahoo and J.A. Lund, *Metall. Trans.*, *4* (1973) 39.
[79] N. Hansen, *Acta Metall.*, *25* (1977) 863.
[80] R.P. Carreker, Jr. and W.R. Hibbard, Jr., *Trans. AIME*, *209* (1957) 1157.
[81] R.J. Arsenault and N. Shi, *Mater. Sci. Eng.*, *81* (1986) 175.
[82] Z.Y. Ma, J. Bi, Y.X. Lu and Y.X. Gao, *Scr. Metall. Mater.*, *29* (1993) 225.
[83] R.J. Arsenault, in R.K. Everett and R.J. Arsenault (eds.), *Metal Matrix Composites: Mechanisms and Properties*, Academic Press, Boston, MA, 1991, pp. 79–100.